



HAL
open science

Analysis of the Total Instantaneous Blockage accident consequences in the innovative inherently-safe CADOR SFR core

Thibaut Rahm, Jean-Baptiste Droin, Nathalie Marie, Frédéric Bertrand,
Amandine Marrel

► To cite this version:

Thibaut Rahm, Jean-Baptiste Droin, Nathalie Marie, Frédéric Bertrand, Amandine Marrel. Analysis of the Total Instantaneous Blockage accident consequences in the innovative inherently-safe CADOR SFR core. Nuclear Engineering and Design, 2019, 348, pp.78-89. 10.1016/j.nucengdes.2019.04.019 . cea-02510329

HAL Id: cea-02510329

<https://cea.hal.science/cea-02510329>

Submitted on 17 Mar 2020

HAL is a multi-disciplinary open access archive for the deposit and dissemination of scientific research documents, whether they are published or not. The documents may come from teaching and research institutions in France or abroad, or from public or private research centers.

L'archive ouverte pluridisciplinaire **HAL**, est destinée au dépôt et à la diffusion de documents scientifiques de niveau recherche, publiés ou non, émanant des établissements d'enseignement et de recherche français ou étrangers, des laboratoires publics ou privés.

Analysis of the Total Instantaneous Blockage accident consequences in the innovative inherently-safe CADOR SFR core

Thibaut Rahm^a, Jean-Baptiste Droin^{a,*}, Nathalie Marie^a, Amandine Marrel^a

^a*CEA, Cadarache*

Abstract

Within the framework of long term prospective studies, an inherently-safe Sodium Fast Reactor (SFR) core, named CADOR (Core with Adding DOppleR effect), is studied at CEA (French commissariat à l'énergie atomique et aux énergies alternatives). This core concept mainly relies on its enhanced Doppler effect. The behavior of this innovative core design, when facing severe accident transients resulting from unprotected sequences, is currently assessed in order to demonstrate the benefits of such a core configuration in terms of margins with respect to multiple safety criteria. This paper focuses on the Total Instantaneous Blockage (TIB) sequence that has been simulated out with the analytical tool BETINa. This is a fast-running tool based on the coupling between low-dimensional models and advanced statistical techniques. Firstly, a reference transient study enables to highlight the slow kinetic of this transient in comparison with more conventional homogeneous cores such as SuperPhenix. This is explained by the low power of the CADOR sub-assemblies in this core concept and to their high thermal inertia compared to previous SFR cores. Then, a parametric analysis allows to further understand the core behavior, focusing on the influence of the thermal or hydrodynamic propagation of molten material to the neighbouring sub-assemblies and on the axial location of the hexcan failure. These parameters are indeed identified as explaining a large part of the total

*Corresponding author

Email address: jean-baptiste.droin@cea.fr (Jean-Baptiste Droin)

variability of the final molten fuel mass. Finally, a complete statistical study based on the variation of 27 uncertain input parameters enables to identify the most influential parameters on the final core degradation.

Keywords: SFR core, severe accident, TIB, uncertainty propagation, global sensitivity analysis

1. Introduction

The CADOR core (Core with Adding DOppleR effect) is an innovative Sodium Fast Reactor (SFR) core design, aiming at improving the intrinsic natural behavior of the reactor when facing overpower transients [1]. It is especially
5 featured by an enhanced Doppler effect achieved through a proper core design. To quickly cope with the behavior of such a new core design when facing accidental transients without using complex multi-physic codes (SAS, SIMMER [2]), several fast-running design-oriented tools have been developed at CEA. Indeed, mechanistic tools, that require extended CPU time for each calculation
10 (up to several days/weeks), are not suitable in a context of preconceptual design phase where many core features might change rapidly. Moreover, they do not allow sensitivity studies and uncertainty treatment approaches that are yet relevant in such design process. Since they are validated against experimental results, the use of fast-running tools offers the possibility to test a wide range
15 of input parameters to quantify safety margins with respect to multiple safety criteria. An approach based on margins assessments with design-oriented tools thus enable to take into account safety features in early preconceptual design phases.

In the past, the need of this approach based on low dimensional physical
20 modellings has already been highlighted. Indeed, in the eighties an international consensus [3, 4] was reached that, the mechanistic approach is not sufficient to assess safety demonstration due to the complexity of severe accidents phenomenology. In France, an approach combining physical events modelling with uncertainties treatment has been developed for PWR severe accident analysis

25 [5]. In Japan, the methodology development review of Level 2 PSA (probabilistic safety assessment) for SFR [6, 7] also underlined the need to consolidate these studies with analytical methodologies. An analogous approach has been followed by the IGCAR (Indira Gandhi Centre for Atomic Research) to investigate the core damage due to the TIB (Total Instantaneous Blockage) of a SFR
30 fuel sub-assembly (SA) [8]. The authors concluded that, for the elaboration of parametric studies, simplified and robust models that capture the essential features of the event progression should be preferred to more sophisticated and mechanistic tools.

Within this international context, the development of such fast-running tools
35 has been undertaken at French CEA to complete the deterministic SFR safety demonstration with sensitivity studies and uncertainties propagation analyses. For this purpose, significant phenomena were identified and modelled for each boundary accidental sequence, mainly based on literature and test reports. Such physical tools were created to simulate Loss Of Flow [9, 10], OverPower
40 Transients [11], Disruptive Core Accidents expansion phases [12] and, more specifically in the scope of this paper, TIB transients [13]. As the CADOR core is intrinsically characterized by an enhanced Doppler effect in transient conditions, it is safer than more conventional cores regarding loss of flow or overpower transients. However, as the TIB transient does not implicate a significant core
45 power evolution, the Doppler effect does not play a significant role for this transient. Added to the fact that the CADOR SAs are innovatively designed, this makes this unprotected sequence study of a particular interest in CADOR.

The section 2 of the paper firstly describes the CADOR core design and specific features. Then, the TIB transient phenomenology is tackled (section 3)
50 as its modelling in the analytical tool (section 4). A reference TIB simulation is analyzed in section 5. Finally, parametric and statistical studies are both discussed in sections 6 and 7, enabling to highlight conclusions and prospects as mentioned in section 8.

2. The CADOR core

55 The CADOR core conception aims at being the most efficient as possible to prevent fuel meltdown during Unprotected Transient OverPower (UTOP) [1]. For this purpose, the core design is based on a reinforced Doppler constant K_D provided by the presence of beryllium pins inside the SAs. The beryllium is indeed chosen to moderate the neutron flux spectra towards the resonance
 60 absorption peak of ^{238}U . Furthermore, another way to strengthen the Doppler effect in transient conditions is to decrease the nominal temperature of the fuel T_{fuel}^0 . The increased heating amplitude of the fuel pins during overpower transients (ΔT_{fuel}) indeed leads to a larger negative reactivity insertion through the Doppler effect $\Delta\rho_{doppler}$, as visible in equation 1:

$$\Delta\rho_{doppler} = K_D \ln\left(\frac{T_{fuel}}{T_{fuel}^0}\right) \quad (1)$$

65 The core is composed of 615 fuel SAs which are axially homogeneous, in order to achieve a total thermal power of 1500 MW. Each SA is composed of 271 pins, 73 of which are composed of beryllium instead of fuel pellets as displayed in Figure 1. To compensate a quite low linear power in fuel pins (around 100 W/cm), the height of each SA is also increased to reach a total
 70 height of 4.8 m, among which 1.2 m corresponds to the fuel column.

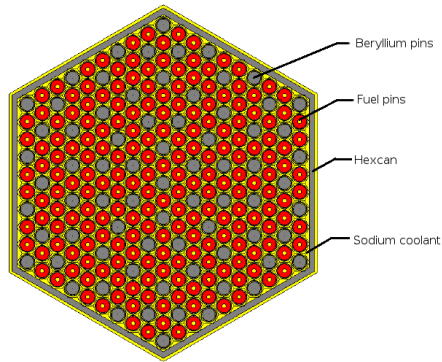


Figure 1: Radial cut of a CADOR sub-assembly with 198 fuel pins and 73 beryllium pins

3. TIB transient

The Total Instantaneous Blockage is a boundary transient of all the sub-assembly faults as it combines both the features of being total (meaning there is no way of detecting the blockage by delayed neutron detection¹ before hexcan failure, due to the absence of sodium stream to convey fission products) and
75 instantaneous.

3.1. Initiation and boiling

The accidental sequence begins with the stop of sodium flow entering at the inlet of the blocked SA. In this SA, the sequence begins with the sodium
80 vaporization, quickly followed by the fuel pins dry out. Due to this dry-out, the following heating up of the pins sharply increases until the clad solidus temperature is reached.

3.2. Pins degradation

Once the clad liquidus temperature is reached, the relocation of molten steel
85 down to the axial solidus temperature location occurs, as shown in Figure 2. The same relocation process then occurs for fuel. Since liquid fuel and liquid steel are non-miscible, two separate phases are formed in the SA as illustrated in Figure 3, the steel pool being on top due its lower density.

3.3. Hexcan failure and end of the transient

90 Concerning the hexcan, its heating-up is mainly induced by conductive and convective heat transfers from both steel and fuel pools. Then, depending on the pressure conditions and on the mechanical strength of the wrapper, hexcan failure may occur quickly. Depending on the tightness of the upper plug (liquid steel that freezes in the upper structures), the propagation of melted material
95 to surrounding SAs can be dynamical or thermal driven mechanisms (or both,

¹System allowing detection and localization of fuel element failure by delayed neutrons conveyed by the coolant to detectors situated above the core.

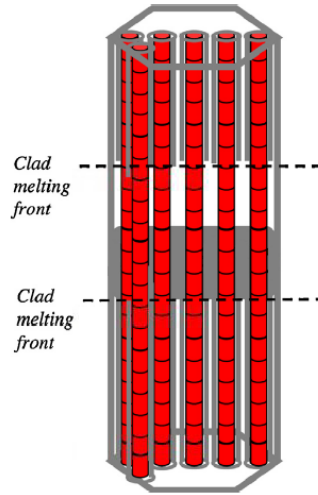


Figure 2: Graphical representation of the faulted sub-assembly during the accidental transient beyond clad melting phase [13]

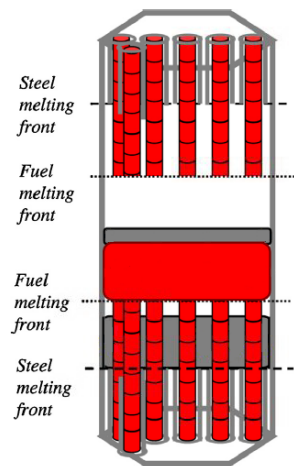


Figure 3: Graphical representation of the faulted sub-assembly during the accidental transient beyond clad and fuel melting criteria [13]

cf. Figure 4). These two types of propagations are further described in section 4.1.5.

Finally, the radial expansion of the molten pools in the core keeps going on until the sodium flow next to the pools is enough to cool the molten materials and until the fuel crust around the pools is thick enough to ensure mechanical stability of the pool.

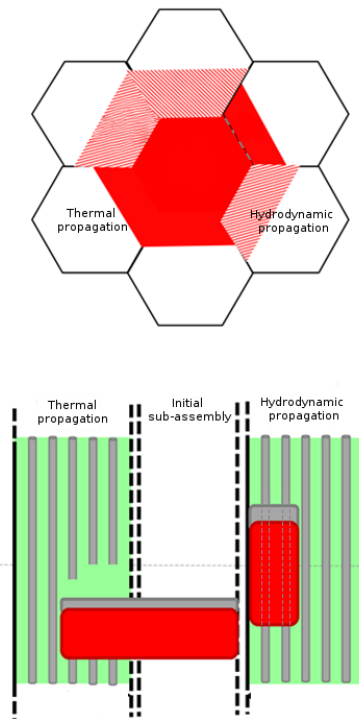


Figure 4: Graphical representation of the molten material progression. [13]

4. Description of the tool

BETINa (French acronym for “Bouchage Total Instantané d’un assemblage de RNR-Na”) is a fast-running tool developed in 2012 at CEA aiming at simulating a TIB transient occurring in a SFR. For validation purpose, simulation

results were compared against SCARABEE tests results [14, 15] in [13]. As more details can be found in [13], this section only aims at briefly recalling the modelling implemented in the tool.

4.1. *Physical modellings*

110 As described below, BETINa is an analytical tool based on the coupling between a 1D modelling for pins and on a 0D modelling for each molten pool, enabling the energy balance equations resolution in each material of the SA. The code is written in MATLAB language, and the numerical resolution method is explicit.

115 4.1.1. *Pins modelling*

One representative fuel pin is modelled through an axial 1D nodalization. Owing to the small conductive heat transfer characteristic time in the pin in comparison to the duration of the transient, the heating-up of the blocked SA is justified to be quasi-adiabatic. In other words, it is justified to consider that 120 the radial temperature differences within the pins, at constant power, remains constant versus time before fuel melting.

Concerning the beryllium pins, they are made of pure metallic beryllium bars enclosed in a steel clad. The cladding geometry is the same as for the fuel pins. The modelling of these pins is implemented on the basis of these 125 assumptions:

- As only one representative fuel pin of a complete SA is calculated in BETINa, only the fraction of Beryllium pins corresponding to this representative fuel pin is calculated.
- As no power is delivered in the beryllium pins, the temperature gradient 130 in both of these metals (steel and fuel) is flat. Added to the fact that they are only composed of metals, these pins can be modelled as an unique homogeneous material. Thermal properties are deduced from the volumetric ratio of each material.

4.1.2. Heating-up and degradation

135 As the TIB is a local accident affecting only a few SAs, its influence on the global core power evolution is neglected in the tool before the reactor scram: the power delivered in the fuel remains at its nominal value, the axial heat flux profile being of cosine shape.

After boiling inception (when the sodium temperature reaches its saturation
140 temperature, around 1173 K at 1 bar), the enthalpy of the sodium is calculated. It is considered that dry-out of the pins occurs for a specified quality deduced from experimental results [15]. Once dry-out is reached, the heat transfer to vapour becomes negligible, as validated by the interpretation of the CESAR experiments [16]. Then, the adiabatic heating-up of the other components (clad
145 and fuel) keeps going until the clad melting criterion is locally reached.

Once the steel melting temperature is reached in one axial mesh, a time delay is calculated for the clad melting, based on the steel latent heat. As observed experimentally (PELUR, CEFUS, BE3+, *cf.* [17]), the volume of the molten steel in the SA within the clad melting zone undergoes mainly gravity
150 relocation. The molten steel volumes then gather at the elevation of the lower clad melting front. Indeed, the PELUR and CEFUS experiments [15, 18] showed that this molten steel freezes at the axial location of the solidus temperature. This relocation results in a stepwise formation of pools in some axial locations.

The same melting and relocation process is implemented for fuel melting.

155 4.1.3. Pools formation

As the relocation process keeps going in the SA, different pools involving various convective heat transfer mechanisms appear inside the hexcan. Another 0D modelling involving thermal balances written on each separated pool (steel and fuel) is considered. The main physical assumptions (validated on past experi-
160 mental works) are exhaustively listed in [13]. Let's remind here that the pools are surrounded by their own crust, and that according to the characteristics of the pool, convective heat transfer coefficients are deduced from experimental correlations such as Bernaz [19], Alvarez [20] and Greene [21].

When in an axial mesh, the beryllium pin is fully melted, it is relocalized
165 in the pool as for a fuel pin. In a first approximation and due to the lack of
thermodynamic data, beryllium is incorporated in the upper steel pool, and the
steel-beryllium mixture is supposed to be homogeneous. Volumetric thermal
properties in the pool (heat capacity, thermal conductivity, etc.) are updated
at each time step depending on its composition.

170 4.1.4. *Hexcan failure*

Finally, to encompass the various hexcan failure modes (over-pressure, local
mechanical defaults or hot points within the wrapper...), the hexcan is assumed
to fail as soon as a given fraction of its thickness is molten. The hexcan failure
initiates the propagation process in the surrounding SAs.

175 4.1.5. *Propagation*

The propagation phenomenology may be driven by thermal or hydrodynamic
mechanisms (or both) [13]. This highly depends on the pressure differential
applied on each side of the hexcan before its failure.

Thermal propagation is controlled by the progressive heating-up and melting
180 of the pins by the molten materials coming from the initial blocked SA.

Hydrodynamic propagation is characterized by the ejection of molten mate-
rial under over-pressure into some neighbouring SAs. This results in the block-
age of some pins in this neighbouring SA: these pins are not cooled anymore with
sodium. The shape of the blocked zone is derived from SIGELCO experiment
185 results [22].

4.1.6. *End of the transient*

The transient simulation goes on until the core situation is safe enough. To
ensure that, all these criteria, that are considered at each time step, should be
verified:

- 190 • all the hydrodynamic propagation are over (the melting of blocked pins is
finished),

- the emergency shutdown has occurred (the power delivered in the core is only the residual power),
- sodium is not boiling in any SA next to molten pools,
- 195 • the fuel crust thickness around each molten pool is sufficient to ensure its mechanical stability.

4.2. Uncertain input data

Some input data are considered as uncertain parameters for two main reasons:

- 200 • the variability associated to the initial conditions and the transient scenario (initial power, time delay for delayed neutrons detection, *etc.*),
- the complexity of physical phenomena and/or of their coupling (quality at dry-out occurrence, void fraction in boiling pools, *etc.*).

Thus, in previous studies dedicated to the SuperPhenix (SPX) core, 27 input parameters were identified as uncertain. To be able to compare results for both
205 cores, the same list is considered here for CADOR. For statistical study purposes, these parameters are associated with probability density laws as specified (and justified) in [13]. When needed, these laws were adjusted for the parameters to match to the CADOR core conditions (pressure, temperature, mass
210 flow rates, *etc.*). Finally, the definition and the density law of each uncertain parameter can be found in Table 1.

5. Reference TIB simulation

In order to get an idea of the reference behavior of the CADOR core during a TIB transient, this section describes the progress of such a transient using
215 the median value of each of the 27 uncertain parameters (Table 1). Results are also compared to the SPX core results from [13]. The main characteristic times (first sodium boiling, clad and fuel melting, hexcan failure, pool unification and

Definition	Probability distribution	Distribution parameters			
		P1	P2	P3	P4
Input data and physical properties					
(1) SA Fuel power variation (burn-up) [W]	Truncated normal	0	0.04	0.34	0.21
(2) Density of fuel [$kg.m^{-3}$]	Triangular	7220	9500	10800	
(3) Density steel [$kg.m^{-3}$]	Triangular	6900	7600	7960	
(10) Density of sodium [$kg.m^{-3}$]	Uniform	750	870		
(4) Heat capacity of fuel [$J.kg^{-1}.K^{-1}$]	Uniform	380	500		
(5) Heat capacity steel [$J.kg^{-1}.K^{-1}$]	Uniform	600	800		
(11) Heat capacity of sodium [$J.kg^{-1}.K^{-1}$]	Uniform	1200	1400		
(6) Conductivity of fuel [$W.m^{-1}.K^{-1}$]	Uniform	3	4		
(7) Conductivity of steel [$W.m^{-1}.K^{-1}$]	Uniform	15	20		
(8-9-12) Latent heat variations for fuel (average: 2.82×10^5), for steel (average: 3×10^5), for sodium (average: 3.86×10^6) [$J.kg^{-1}$]	Truncated normal	0	0.1	0.2	0.2
Modelling variables					
(13) Quality at dry-out occurrence [dimensionless]	Truncated normal	0.22	0.076	0	0.8
(14-15) Void fraction in boiling pools of fuel, of steel, respectively (if empty volume remaining) [dimensionless]	Uniform	0.01	0.99		
(16-17-18-19-20) Nusselt number variations around the value given by the correlations of Alvarez for steel, of Greene for fuel, and of Lyon for sodium.	Truncated normal	0	0.2	0.6	0.6
(21) Time delay for delayed neutron detection [s]	Triangular	25	35	105	
(22) Fraction of the hexcan thickness to melt before failure [dimensionless]	Triangular	0.5	1.5	2	
(23) Aspect ratio of the form taken by the ejected material in hydrodynamic propagation. From SIGELCO data: [8,3 6,8 8,8 8,3]	Truncated normal	8.05	0.866	1	10
(24) Propagation mode: Number of neighbour SAs affected by hydrodynamic propagation	Discrete Uniform (entire value)	0	6		
(25) Fuel pool height underneath the failure location over the total pool height [dimensionless] (SCARABEE BF2, BF3) (Papin, 1990)	Triangular	0	0.75	1	
(26) Critical crust thickness (mechanic stability) [mm]	Triangular	1	2	5	
(27) Sodium velocity in the neighbour SA [$m.s^{-1}$] (coolability criterion)	Triangular	1	2.1	8	
With :					
Probability distribution	Parameter P1	Parameter P2	Parameter P3	Parameter P4	
Uniform	Minimal value	Maximal value			
Triangular	Minimal value	Modal Value	Maximal value		
Truncated normal	Mean	Standard deviation	Minimal value	Maximal value	

Table 1: Uncertain inputs parameters and their associated probabilistic distribution law

	CADOR	SPX
Time of first boiling (<i>s</i>)	13.1	2.6
Time of first clad melting (<i>s</i>)	23.6	6.2
Time of first fuel melting (<i>s</i>)	40.6	7.4
Time of hexcan failure (<i>s</i>)	77.4	18.3
Time of pool unification (<i>s</i>)	415.1	31
Time of end of transient (<i>s</i>)	415.2	295
Molten fuel mass at the end of transient (<i>kg</i>)	244	439
Equivalent molten sub-assemblies at the end of transient	2.2	4.8

Table 2: Progress of a TIB reference transient inside a CADOR and a SPX core sub-assembly with median value of uncertain parameters - $t = 0s$ is the instant of the blockage

end of transient) are summarized in Table 2. Evolution of melted fuel mass for the CADOR case can also be seen in Figure 5.

220 5.1. CADOR results

In the CADOR core, the TIB results in the first melting of the fuel at 40 *s*. However, the formation of a fuel molten pool in the SA only starts when the melting front reaches the external face of the fuel pin, at around 50 *s*. From this moment, the pool grows axially until the hexcan failure that occurs at 77 *s*.
225 Molten materials are then ejected in neighbouring SAs². At this time, we can observe a loss of molten fuel mass in Figure 5, because the considered variable does not keep track of the molten mass inside SAs undergoing hydrodynamic propagation.

In the neighbouring SAs, melting of the pins progresses until reaching 140 *kg*
230 of molten fuel at around 130 *s*. Then, 52 *s* after the TH failure (*i.e.* 129 *s* after the TIB initiation), emergency shutdown occurs due to the detection of delayed neutrons above the core. This implies a sharp decrease of the power delivered in

²Thermal propagation in 3 SAs, hydrodynamic propagation in the 3 others as the median value of the 24th parameter (see Table 1) is considered for this reference transient study.

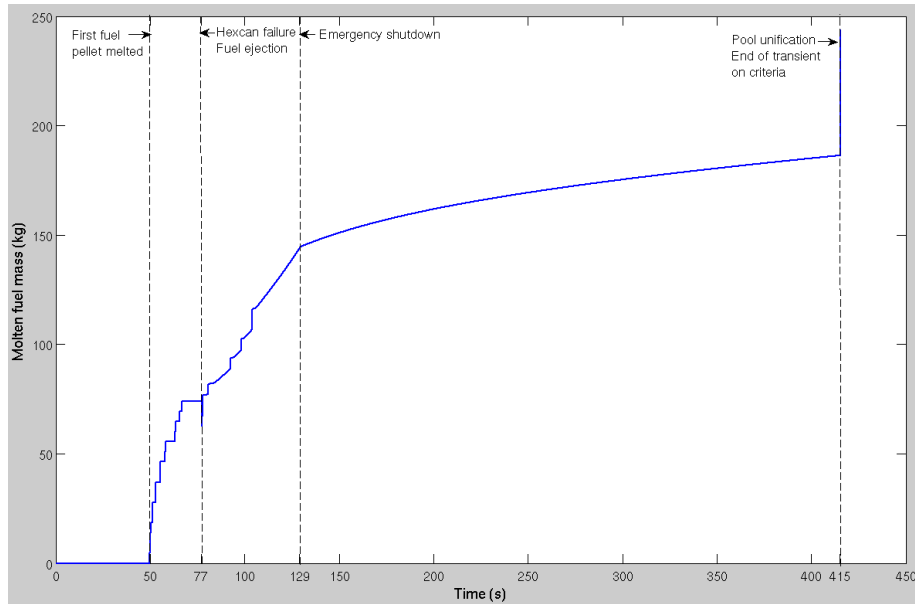


Figure 5: Evolution of molten fuel mass during TIB transient considering median values for uncertain parameters

the fuel pins (residual power only), and thus a slowdown of the total molten mass evolution, clearly visible in Figure 5. However, the formation of the fuel pool still progresses for more than 250 s. At around 415 s, hydrodynamic propagations in the neighbours are over. At this moment, the molten fuel masses in these 3 SAs are finally added to the pool that grows thermally in the core (which is plotted in Figure 5). As the end of hydrodynamic propagation in the core is the last of the criterion listed in paragraph 4.1.6 to be reached, the core is stable and safe enough for the simulation to be ended.

5.2. Differences with SPX results

The degradation sequence during TIB transients is characterized by a slower kinetic in CADOR than in previously studied cores (like SPX, as described in [13]). This is due to:

- the quite low nominal power of each SA in CADOR (around 2.5 MW instead of around 5 MW in SPX),

- the thermal inertia of the beryllium pins in addition to the fuel ones in CADOR.

This is why sodium boiling occurs at 13 s followed by first fuel melting at 40 s and finally hexcan failure at 77 s in CADOR, compared respectively to 2 s, 7 s and 18 s in SPX. The same conclusion can be drawn after the hexcan failure. Indeed, the time needed to melt trapped materials inside the SAs undergoing hydrodynamic propagation is largely increased in CADOR for the same reasons. Thus, it ends at 415 s in CADOR (when all the ending criterion are reached) while it only ends at 31 s in SPX (while thermal propagation keeps going on). Under this fast kinetic in SPX, the total molten fuel mass in SPX is higher in SPX than in CADOR (439 kg instead of 244 kg). Molten mass values in CADOR will be further discussed in section 7.2.

6. Parametric studies

The reference transient simulation is presented in section 5. However, the core behavior may evolve differently if some key parameters are varied as highlighted in [13]. In this section, some parametric studies are presented about two parameters that were identified as key parameters in [13]. These parameters are the number of SAs undergoing hydrodynamic propagation and the height of hexcan failure. These studies are conducted in a one-at-a-time manner, meaning that all the parameters that are not varied are fixed to their median value.

6.1. Number of sub-assemblies under hydrodynamic propagation

This parameter, denoted NbAV, is varied between 0 and 6. $NbAV = 0$ means that thermal propagation occurs in the 6 neighbouring SA. Conversely, $NbAV = 6$ means that the propagation is hydrodynamic in all each of the 6 neighbouring SAs. Figure 6 illustrates the evolution of the number of equivalent molten SAs at the end of the transient as a function of the number of SAs undergoing hydrodynamic propagation.

It is possible to identify three behaviors:

- 275 • When $NbAV = 0$: all the neighbouring SAs are undergoing thermal propagation. As there is no hydrodynamic propagation (which is really slow in CADOR), the core reaches quickly a stable and safe state, at only 154 s. Only a few SAs are molten (1.57 equivalent molten SA).
- 280 • When $0 < NbAV < 6$: the transient degradation is similar to the one described above as reference in section 5, with both thermal and hydrodynamic propagations towards the neighbouring SAs. As the hydrodynamic propagation is slow due to trapped beryllium pins, the core reaches a stable state lately, at around 415 s. During this delay, the thermal propagation is still progressing, explaining the increased value of molten SAs for these simulations. For high values of NbAV, there is less molten fuel by thermal propagation in neighbouring SAs. This why we can observe a slow decrease of the number of molten SAs with an increase of NbAV.
- 285 • When $NbAV = 6$: all the neighbouring SAs are undergoing hydrodynamic propagation. Despite a long transient (still around 415 s), the absence of thermal propagation significantly reduces the expansion of the pool in the core. Hydrodynamic propagation is slow, but only affects a few trapped pins in each surrounding SA. Then, this absence of thermal expansion during hydrodynamic propagation explains the low number of molten SAs in this simulation (1.42).

295 It can be concluded from this first parametric study that, in CADOR, the number of neighbouring SA undergoing hydrodynamic propagation actually drives the duration of the transient before reaching a stable and safe state, while thermal propagation mostly drives the radial expansion of the fuel pool in the core.

300 6.2. Height of hexcan failure

This parameter, denoted Z_{pic} , defines the location of the hexcan failure in regard to the total height of the pool (fuel + steel). $Z_{pic} = 0$ means that the failure occurs at the bottom part of the pool while $Z_{pic} = 1$ means it occurs

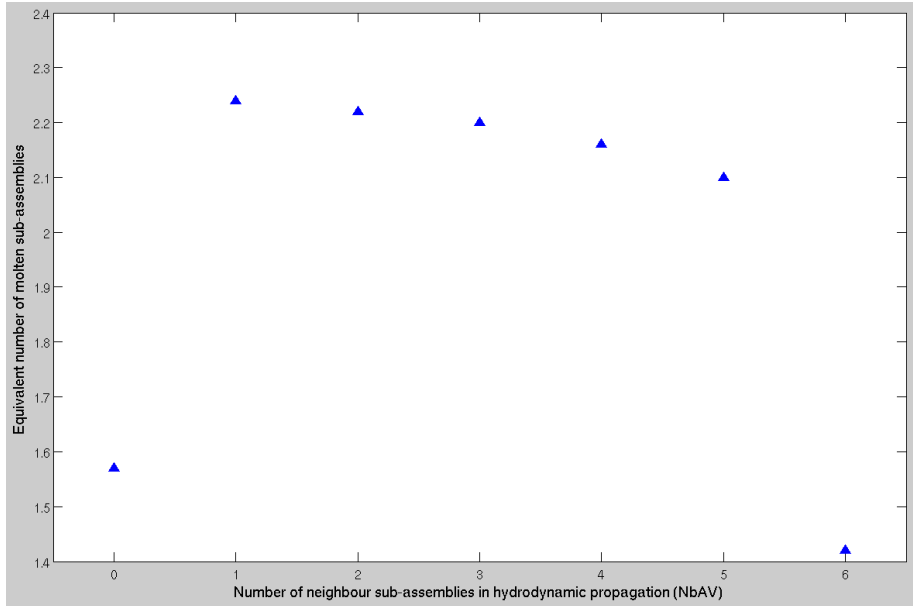


Figure 6: Evolution of the final number of equivalent molten sub-assemblies with the NbAV parameter

at the top part. In SCARABEE experiments [15, 21], this failure is shown to
 305 happen at the location of maximum lateral heat flux toward the hexcan. How-
 ever, due to experimental uncertainties, this location is treated as an uncertain
 parameter in this paper. The evolution of the final number of molten SAs is dis-
 played in Figure 7. A threshold corresponding to $Z_{pic} = 0.73$ is clearly visible,
 it corresponds to the axial limit between the fuel molten pool and the upper
 310 steel pool (molten clad pool):

- Under 73% of the pool height, the hexcan failure occurs in regard to the fuel molten pool. Therefore, when Z_{pic} increases, the mass of molten fuel ejected hydrodynamically toward the neighbours decreases in favour of the mass which progresses thermally. Thus, the total molten fuel mass at the
 315 end of the transient increases.
- Above 73% of the pool height, the hexcan failure happens in regard to the upper steel pool (molten clad). Increasing the height of failure does

not increase anymore the amount of molten fuel left in the initial SA that progresses only thermally. There is only some molten steel which is ejected to neighbours. And increasing the height of failure decreases this ejected steel volume, thus decreasing the number of pins blocked in the neighbours. This explains the slight decrease of molten SAs for high values of Z_{pic} .

Finally, the higher mass of molten fuel is obtained when the hexcan failure occurs at the axial limit between the fuel and the steel pools. This maximizes the fuel thermal propagation while ejected molten steel blocks quite a high number of pins in neighbouring SAs.

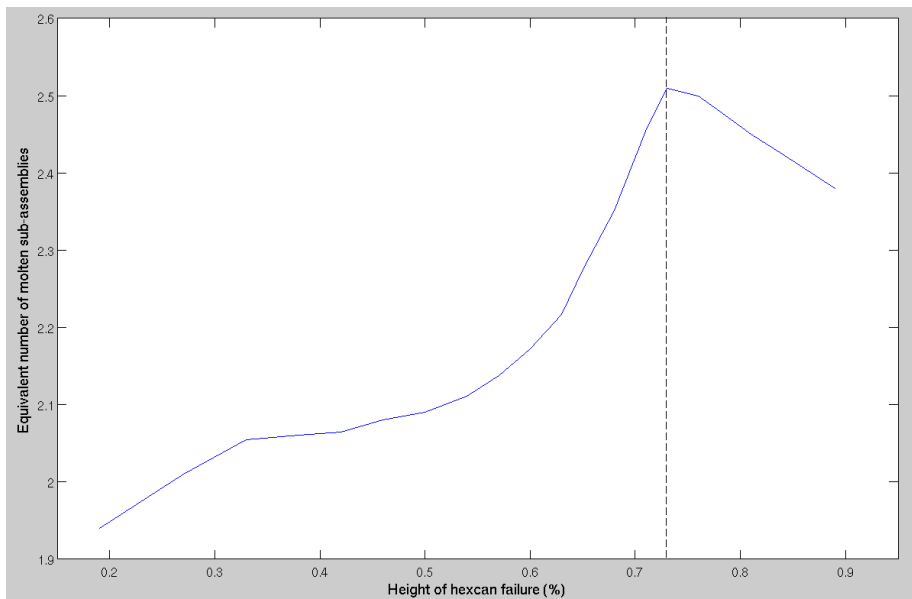


Figure 7: Evolution of the final number of equivalent molten sub-assemblies with the Z_{pic} parameter

7. Statistical studies

The One-at-a-Time parametric studies enabled to highlight some physical thresholds related to the mechanisms driving the propagation toward the neigh-

bouring SAs and to the height of hexcan failure. In addition, we now perform a statistical study where all the uncertain input parameters are considered as random input variables of the TIB simulator. In a probabilistic framework, they are characterized by their probability density functions. The objective is to propagate these uncertainties of inputs and assess how they can affect the simulator forecasts and more specifically the outputs of interest, namely the final number of molten SAs and the ending time of the transient.

7.1. Uncertainty quantification and experimental design

To efficiently investigate the domain of variation of the uncertain parameters listed in Table 1, we use a space-filling design (SFD) of N experiments, providing a full coverage of the high-dimensional input space. Among classical SFD, a Latin Hypercube Sample (LHS, [23]) with optimal space-filling and good projection properties would be well adapted. More precisely, as recommended in [24] and as already used in [25] for SPX, we use a low-discrepancy LHS ([26]), which minimizes a criterion based on a non-uniformity measure (the discrepancy). From an optimized LHS, $N = 1000$ simulations of BETINa are thus performed and constitute the learning sample. Note that the input values are sampled following the probabilistic distributions defined in Table 1.

Remark 7.1. The number N of simulations is a compromise between the CPU time required for each simulation and the number of input parameters. For uncertainty propagation and metamodel-building purpose, some thumb rules propose to choose N at least as large as 10 times the number of inputs.

7.2. CADOR results

The main outputs of interest are the final number of equivalent molten SAs and the ending time of the transient, denoted N_{bMSA} and t_{final} respectively. The histogram of the observed values for these two outputs are displayed in Figures 8 and 9, respectively. A kernel density estimator ([27]) of the data is provided to estimate the probability density function. Descriptive summary statistics are also given in Table 3. It can be seen that the mean value of

360 NbMSA in CADOR is around 2.0 with a quite weak standard deviation of 0.4.
Moreover, the observed values of NbMSA lie between a minimum of 1.03 and a
maximum of 3.8. From the histogram t_{final} given by Figure 9, it can be seen
that the duration of the transient can take a very wide range of time from 88 s to
3611 s. Furthermore, the probability distribution of t_{final} is highly asymmetric,
365 the median value being 176 s while the mean one is 561 s.

7.3. Comparison with SPX results

Two main conclusions can be drawn from these results (in comparison with
previous studies for SPX [13]):

- The number of molten SAs is lower in CADOR than in SPX (mean value
370 of 2.0 instead of 5.5, maximum value of 3.8 instead of 37, etc.). This is
consistent with section 5.
- The variability of this number is also much lower in CADOR than in SPX
(standard deviation of 0.4 instead of 7.5).

The reduced number of extreme values is linked to the fact that, in CADOR
375 simulations, the last criterion to be reached before reaching a stable and safe
state is almost always the ending of the hydrodynamic propagation. For more
powerful SAs such as in SPX, sodium boiling and fuel crust criteria are more
difficult to reach and add variability to ending time results. Moreover, due to
the faster kinetic of the transient in SPX (still related to the higher power in
380 each SAs), a same variability on ending times results in more molten SAs for
SPX than for CADOR, explaining the large difference in standard deviations
between the two core concepts.

7.4. Global sensibility analysis

Global Sensitivity Analysis (GSA, [28]) is an invaluable tool to identify the
385 most influential uncertain parameters, their possible significant interactions, and
the non-influential parameters. A widely used GSA approach is the one based
on variance decomposition, leading to the definition of Sobol' indices ([29]). It

	Final NbMSA	$t_{final}(s)$
Mean	2.02	176
Standard deviation	0.4	577
Median	2.05	561
Min	1.04	88
Max	3.8	3611

Table 3: Summary statistics of TIB transient outputs: final number of equivalent molten sub-assemblies (NbMSA) and time of end of transient (t_{final})

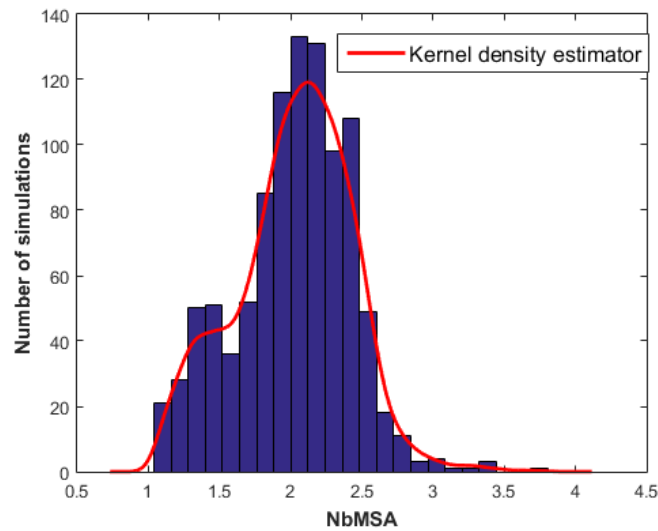


Figure 8: Probability distribution of the number of equivalent molten sub-assemblies (NbMSA) over the 1000 simulations in the CADOR core (in red, a kernel-based estimator of probability density)

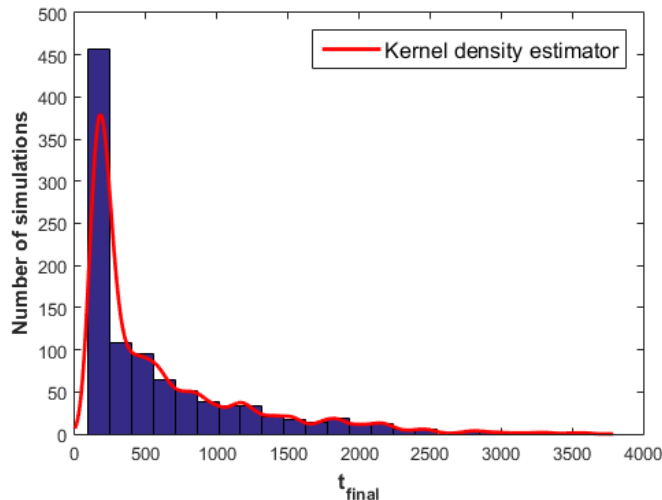


Figure 9: Probability distribution of the time of end of transient (t_{final}) over the 1000 simulations in the CADOR core (in red, a kernel-based estimator of probability density)

accounts for the whole variation range of the inputs and tries to explain the output variance on the basis of input uncertainties. However, such quantitative

390 GSA studies require several thousand simulations. Even if BETINa is a fast-running tool, it could still be considered as too time expensive to be directly used to estimate Sobol' indices. A solution could be to approximate the BETINa outputs by a CPU inexpensive mathematical function, called surrogate model or metamodel ([30]). This metamodel is built from a set of simulations and

395 must be as representative as possible of the simulator in the variation domain of its uncertain parameters, with good prediction capabilities.

7.4.1. Approximation with Gaussian process metamodel

Among the metamodels classically used in computer experiments, the Gaussian process (Gp) model has shown strong advantages and capabilities in the

400 framework of modeling of numerical simulators (see [31], [32] or [33]). Following the same methodology as [25], a Gp metamodel is estimated from the 1000 simulations for the number of equivalent molten sub-assemblies (NbMSA).

To evaluate the accuracy of the metamodel, we use the predictivity coefficient

Q^{23} . In practice, the Q^2 is computed by cross-validation on the learning sample.
405 We obtain here a Q^2 of 0.92 for the Gp metamodel, which illustrates its very good accuracy. Note that a linear regression metamodel has been also tested and yields very poor results (Q^2 around 0.09). This illustrates the strong non-linearity of the output NbMSA with respect to the inputs, hence the interest of using more complex metamodel such as Gp.

410 7.4.2. Computation of Sobol' indices with metamodel

In order to identify the most influential uncertain parameters on NbMSA, we compute Sobol' indices ([29]). Based upon the functional variance decomposition of any integrable function, these sensitivity measures determine how to share the output variance resulting from each input variable (first order Sobol' indices) or interaction between input variables (higher order indices). A first order index measures the part of the output variance explained by one input alone. A second-order index gives the part of variance due to the interaction effect between two inputs, independently from their effects alone. In an equivalent way, higher order indices can be defined. All the Sobol' indices are all
415 included in the interval $[0; 1]$, their sum is one in the case of independent input variables and their interpretation is natural: the larger the index value, the more influential the input related to this index.
420

In this paper, to estimate the Sobol indices, we used Monte Carlo-based formulas of [28] and made ten thousands simulations with the Gp metamodel.
425 Results obtained for NbMSA are summarized in Table 4.

They show that the number of neighbouring SAs affected by hydrodynamic propagation (denoted NbAV, as a reminder) accounts for almost all the variability of the NbMSA with a first-order index of 0.55 and a total index of 0.81. This parameter was also the most important in the SPX studies [13] but to a lesser
430 extend (first-order and total Sobol' indices of 0.15 and 0.54, respectively). The

³which corresponds to the coefficient of determination in prediction and gives us the percentage of explained output variance

other parameters have very low first-order index (therefore not influential alone) while being more influential in interaction with nbAV. These non-negligible parameters are the time of delayed neutron detection, height of hexcan failure (Zpic), thickness of hexcan enabling the failure and variation of nominal power (corresponding to the uncertainty relative to the blocked SA position in the core). These variables are similar to those found during the SPX studies [13].

Input variable (cf. Table 1)	Sobol' indices	
	1 st order Index	Total index
1 - Fuel power variation	0.02	0.18
21 - Time delay for delayed neutron detection	0.05	0.26
22 - Fraction of the molten hexcan thickness to melt before fraction	0.02	0.06
24 - Number of neighbour SAs affected by hydrodynamic propagation	0.55	0.79
25 - Height of hexcan failure	0.02	0.22
Interaction between variables	2nd order Index	
1×21×24	0.08	
21×24	0.06	
25×24	0.13	

Table 4: Summary of significant Sobol' indices for the final number of equivalent molten sub-assemblies (indices estimated with the Gp metamodel).

7.4.3. Study of primary effects of significant inputs

In the light of the GSA results, we focus now on the analysis of the primary effect of the most influential input (namely NbAV) on the final molten fuel mass, and on its stronger interaction (namely the one with Zpic). The objective is to complete the results of parametric studies in Sections 6.1 and 6.2.

From the 1000 simulations of the learning sample, the scatterplot of the output with respect to NbAV is first displayed in Figure 10. Thanks to the Gp

metamodel, the conditional mean effect of NbAV is also estimated via condi-
445 tional means⁴. The estimated conditional mean effect of NbAV is given in red
solid line, in Figure 10. Even when all the other parameters vary, the mean ef-
fect of NbAV is clearly the same as the one identified in One-At-A-Time studies
of Section 6.1, with three clearly different behaviors.

The same analysis is done for Zpic. The results are given by Figure 11. It
450 appears that the effect of Zpic can be divided into three distinct sub-behaviors
depending on the value of NbAV, this being consistent with the estimated Sobol'
indices (significant second-order index between NbAV and Zpic). If NbAV is
different from 0 and 6, the global effect of Zpic is the same as the one described
in the parametric studies in section 6.2: NbMSA increases with Zpic until a
455 maximal value reached for Zpic around 0.8 and decreases after. On the other
hand, when combined with a value of NbAV of 6 (*i.e.* if propagation is only
hydrodynamic), the influence of Zpic is completely different: NbMSA globally
decreases with Zpic. This is explained by the fact, as there is no thermal prop-
agation in the neighbouring SAs, the total mass of molten fuel is only governed
460 by the volume of fuel that is dynamically projected in the neighbours. As the
latter indeed decreases with Zpic, so does the final molten fuel mass. Finally,
when NbAV is equal to 0 (*i.e.* when there is no hydrodynamic propagation in
the neighbours), Zpic has no mean effect on NbMSA because the duration of
thermal propagation does not depend on the volume that is projected into the
465 neighbours (on the contrary to hydrodynamic propagation).

8. Conclusions and Prospects

The main objective of this work is to assess the CADOR core behavior
when facing a TIB transient, only accidental sequence for which this core does
not benefit from its Doppler effect enhanced by design. For this purpose, the

⁴The conditional effect according to a given input (here NbAV) is a function depending
only on the value of the input, which provides information on the influence of each input alone
and independently from the others (see [13] for more details).

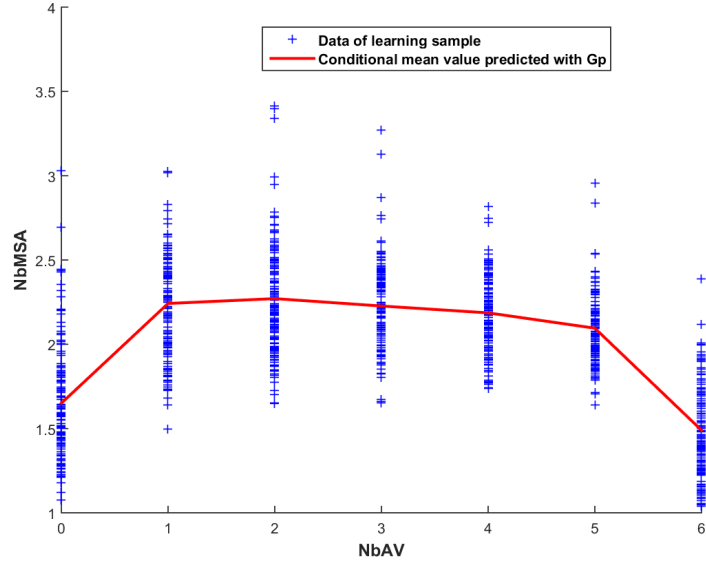


Figure 10: Repartition of the number of molten sub-assemblies on 1000 simulations w.r.t. NbAv. In red: the mean value conditionally to NbAv is estimated with the Gp metamodel.

470 previously developed BETINa tool has been updated in order to accommodate this innovative core specificities (in particular the presence of beryllium pins inside the sub-assemblies).

In section 5, a reference TIB analysis showed that CADOR benefits from a slow transient kinetic related to its low nominal power as to the presence of cold and non-heated beryllium pins. Thus, the TH fails only after 80 s instead of 30 or 40 s for more conventional core (as SPX), and the molten fuel mass at the end of the transient is also lower. This slower kinetic however implies longer transients before reaching a stable and safe core state (around more than 400 s in CADOR against 300 s in SPX).

480 Parametric studies also enabled to highlight specific phenomena in section 6. In particular, the fuel mass inventory is shown to be higher in case of both thermal and hydrodynamic propagation of molten materials to the neighbouring SAs. If this propagation is driven by one mechanism only, the fuel mass

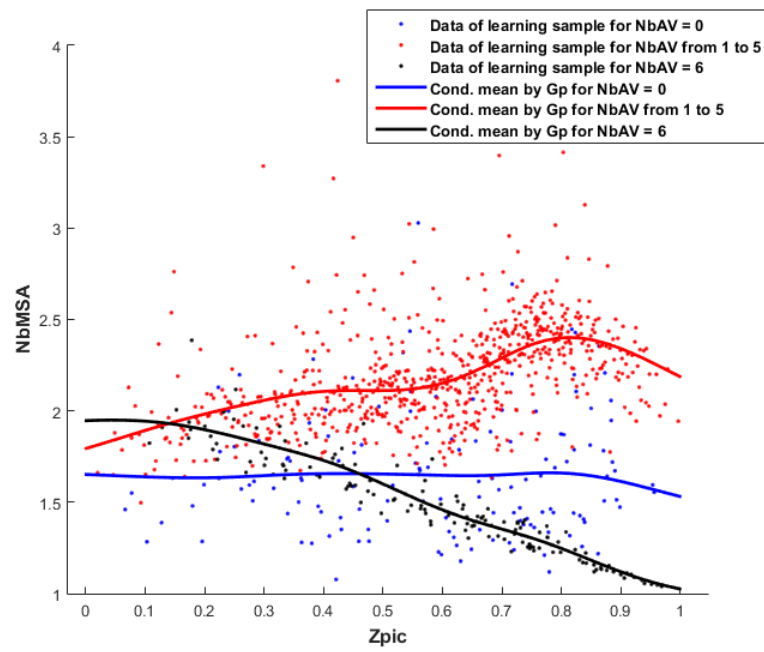


Figure 11: Repartition of the number of molten sub-assemblies on 1000 simulations w.r.t. Z_{pic} and clustered according to NbAV. In solid line: the mean value conditionally to Z_{pic} and according to NbAV is estimated with the Gp metamodel.

inventory is quite low. Then, concerning the location of the hexcan failure, the
485 worst case (leading to high molten mass inventories) is when the failure occurs
at the axial limit between the fuel pool and the steel one.

A statistical analysis of the transient was also carried out in section 7 in order
to assess safety margins and to identify the most influential input parameters.
This study was based on the 27 uncertain parameters (that were previously
490 identified in [13] for the SPX core) and performed through a space-filling design
of 1000 BETINA simulations. As expected in the light of the reference
TIB analysis, the average number of equivalent molten SAs (NbMSA) is lower
in CADOR than in SPX (2.1 in CADOR against 2.6 in SPX). The fact that
the transient is characterized by a slow kinetic also explains a largely reduced
495 variability of the results (standard deviation of 0.4 instead of 7.5 in SPX). Finally,
the global sensitivity analysis of the number of molten sub-assemblies was
performed on the basis of an accurate Gaussian process metamodel. This resulted
in the identification of one input parameter explaining most of the output
variability: the thermal or hydrodynamic propagation to the neighbouring SAs
500 after hexcan failure. Alone, it explains 55 % of the overall variability concerning
molten fuel mass. Coupled to other input parameters (especially axial location
of hexcan failure and time delay before delayed neutron detection), it explains
26 % more. Thus, this parameter is related to 81 % of this output variability.

The main prospect of this work deals with the elaboration of a neutronic
505 kinetics model that would compute the power evolution in a function of the
molten materials distribution in the core. Even if it should not be significant
for most of the simulations, this may have an impact for a few simulations
leading to a high number of molten SAs.

Acknowledgment

510 The authors would like to thank the Nuclear Support and Innovation Division
of CEA and its industrial partners AREVA and EDF, which supported and
contributed to this work.

References

- [1] A. Zaetta, B. Fontaine, P. Sciora, R. Lavastre, M. Pelletier, G. Mignot,
515 A. Jankowiak, CADOR "Core with Adding DOppleR effect" CONCEPT,
Application to Sodium Fast Reactors, under review.
- [2] S. Kondo, K. Morita, Y. Tobita, K. Kamiyama, D. Brear, E. Fischer,
et al., SIMMER-III: A computer program for LMFR core disruptive ac-
cident analysis, PNC ZN9410 96-207, O-arai Engineering Center, Power
520 Reactor and Nuclear Fuel Development Corporation.
- [3] L. Luck, C. Bell, The case of integral core - disruptive accident analysis,
ANS/ENS Fast Reactor Safety Meeting, Knoxville, TN, USA, p. 21.
- [4] F. Martin, Bottled transition phase analysis, Preliminary Report. HEDL-
TME. 78-64.
- 525 [5] B. Iooss, F. Gaudier, M. Marques, B. Spindler, B. Tourniaire, Uncertainty
assessment in severe nuclear accident scenarios, First International Confer-
ence on Advances in System Simulation (2009) 94–99.
- [6] R. Nakai, T. Suzuki, H. Yamano, H. Seino, H. Ishikawa, Development of Se-
vere Accident Evaluation Technology (Level 2 PSA) for Sodium-cooled Fast
530 Reactor (1) Overview of evaluation Methodology Development, ICAPP09,
Tokyo, Japan, May 10-14, 2009.
- [7] H. Yamano, I. Sato, Y. Tobita, Development of technical basis in the initi-
ating and transition phases of unprotected events for Level-2 PSA method-
ology in sodium-cooled fast reactors, Nuclear Engineering and Design 249
535 (2012) 212–227.
- [8] L. Ravi, K. Velusamy, P. Chellapandi, A robust thermal model to investi-
gate radial propagation of core damage due to total instantaneous blockage
in SFR fuel assembly, Annals of Nuclear Energy 62 (2013) 342–356.

- [9] J.-B. Droin, N. Marie, A. Bachrata, F. Bertrand, E. Merle, J.-M. Seiler, Physical tool for unprotected Loss Of Flow transient in a Sodium fast Reactor, *Annals of Nuclear Energy* 106 (2017) 195–210.
- [10] J.-B. Droin, N. Marie, F. Bertrand, E. Merle-Lucotte, J.-M. Seiler, Analytical modelling of the primary phase of an unprotected loss of flow, NURETH-16, Paper 13036, Chicago, IL, USA, August 30 - September 4, 2015.
- [11] K. Herbreteau, N. Marie, F. Bertrand, J.-M. Seiler, P. Rubiolo, Sodium-cooled fast reactor pin model for predicting pin failure during a power excursion, *Nuclear Engineering and Design* 335 (2018) 279–290.
- [12] X. Manchon, F. Bertrand, N. Marie, M. Lance, D. Schmitt, Modeling and analysis of molten fuel vaporization and expansion for a sodium fast reactor severe accident, *Nuclear Engineering and Design* 322 (2017) 522–535.
- [13] N. Marie, A. Marrel, J.-M. Seiler, F. Bertrand, Physico-statistical approach to assess the core damage variability due to a total instantaneous blockage of SFR fuel sub-assembly, *Nucl. Eng. Des.* 293 (2015) 343–353.
- [14] G. Kayser, J. Charpenel, C. Jamond, Synthesis of SCARABEE-N program, with main results and application to the total instantaneous blockage reactor, *Nucl. Eng. Des.* 128 (1998) 144–185.
- [15] J. Papin, R. Sesny, P. Soussan, J. M. Dougall, The SCARABEE total blockages test serie: synthesis of the interpretation., 7th international fast reactor safety meeting. *Am. Nucl. Soc.* 1, 367-376.
- [16] D.-S. So, J.-M. Seiler, Sodium boiling, dry out and clad melting in a sub-assembly of LMFBR during a total and instantaneous inlet blockage accident, *Proceedings of the 11th Liquid Metal Boiling Working Group*, Grenoble, 23-26 October, 1984.
- [17] J. Papin, Behavior of fast reactor fuel during transient and accident conditions, *Comprehensive Nuclear Materials Elsevier Ltd.*

- [18] J. Papin, J.-M. Seiler, Synthesis of clad motion experiments interpretation: codes and validation, Proceedings of the 2nd International Topical Meeting on Nuclear Reactor Thermal Hydraulics, Santa Barbara (California) January, pp. 11-14, 1983.
- 570
- [19] L. Bernaz, Investigation of natural convection heat transfer to the cooled top boundary of a heated pool, Proceedings of the 9th Topical International Meeting on Nuclear Reactor Thermal-Hydraulics (NURETH-9), San Francisco, California, October, pp. 3-9, 1984.
- 575
- [20] D. Alvarez, P. Malterre, J.-M. Seiler, Natural Convection in Volume Heated Liquid Pools The BAFOND Experiments: Proposal for New Correlations, Science and Technology of Fast Reactor Safety. BNES, London.
- [21] M. Bede, C. Perret, H. Pretrel, J.-M. Seiler, One component, volume heated, boiling pool thermohydraulics., Proceedings of the 6th Topical International Meeting on Nuclear Reactor Thermal-Hydraulics (NURETH-6), Grenoble, France, October, pp. 5-8, 1993.
- 580
- [22] B. Duret, J.-C. Bonnard, Crust instability criteria during transient freezing on anliquid film, Proceedings of the ASME Winter Annual Meeting, Chicago, Illinois, Nov. 27-Dec. 2, 1988.
- 585
- [23] M. McKay, R. Beckman, W. Conover, A comparison of three methods for selecting values of input variables in the analysis of output from a computer code, *Technometrics* 21 (1979) 239–245.
- [24] G. Damblin, M. Couplet, B. Iooss, Numerical studies of space filling designs: Optimization of Latin hypercube samples and subprojection properties, *Journal of Simulation* 7 (2013) 276–289.
- 590
- [25] A. Marrel, N. Marie, M. D. Lozzo, Advanced surrogate model and sensitivity analysis methods for sfr accident assessment, *Reliability Engineering & System Safety* 138 (2015) 232241.

- [26] K.-T. Fang, Wrap-around L_2 -discrepancy of random sampling, Latin hypercube and uniform designs, *Journal of Complexity* 17 (2001) 608–624.
595
- [27] E. Parzen, On estimation of a probability density function and mode, *The Annals of Mathematical Statistics* 33 (3) (1962) 1065–1076.
- [28] A. Saltelli, Sensitivity analysis for importance assessment, *Risk Analysis* 22 (2002) 1–12.
- [29] I. Sobol, Sensitivity estimates for non linear mathematical models, *Mathematical Modelling and Computational Experiments* 1 (1993) 407–414.
600
- [30] K.-T. Fang, R. Li, A. Sudjianto, *Design and modeling for computer experiments*, Chapman & Hall/CRC, 2006.
- [31] J. Sacks, W. Welch, T. Mitchell, H. Wynn, Design and analysis of computer experiments, *Statistical Science* 4 (1989) 409–435.
605
- [32] C. Rasmussen, C. Williams, *Gaussian processes for machine learning*, MIT Press, 2006.
- [33] A. Marrel, B. Iooss, F. Van Dorpe, E. Volkova, An efficient methodology for modeling complex computer codes with Gaussian processes, *Computational Statistics and Data Analysis* 52 (2008) 4731–4744.
610